Pearl-inspired graphene oxide-collagen microgel with multi-layer mineralization through microarray chips for bone defect repair

Chuchao Zhou [a,b], Chao Luo [a], Shaokai Liu [a], Shangxuan Jiang [a], Xin Liu [a], Jialun Li [a], Xinyue Zhang [c], Xiaoyan Wu [c], Jiaming Sun [a,**], Zhenxing Wang [a,*]

[a] Department of Plastic Surgery, Union Hospital, Tongji Medical College, Huazhong University of Science and Technology, Wuhan, 430022, China
[b] Department of Plastic Surgery, Tongren Hospital of Wuhan University (Wuhan Third Hospital), Wuhan, 430060, China
[c] Department of Pediatric, Union Hospital, Tongji Medical College, Huazhong University of Science and Technology, Wuhan, 430022, China

ARTICLE INFO

ABSTRACT

Biomineralization of natural polymers in simulated body fluid (SBF) can significantly improve its biocompatibility, osteoconductivity, and osteoinductivity because of the hydroxyapatite (HAp) deposition. Nevertheless, the superficial HAp crystal deposition hamper the deep inorganic ions exchange in porous microgels, thus gradually leading to a nonuniform regeneration effect. Inspired by the pearl forming process, this article uses the microarray chips to fabricate the multi-layer mineralized graphene oxide (GO)-collagen (Col)-hydroxyapatite (HAp) microgel, denoted as MMGCH. These fabricated MMGCH microgels exhibit porous structure and uniform HAp distribution. Furthermore, the suitable microenvironment offered by microgel promotes the time-dependent proliferation and osteogenic differentiation of stem cells, which resulted in upregulated osteogenesis-related genes and proteins, such as alkaline phosphatase, osteocalcin, and collagen-1. Finally, the MMGCH microgels possess favorable bone regeneration capacities both in cranial bone defects and mandibular bone defects via providing a suitable microenvironment for host-derived cells to form new bone tissues. This work presents a biomimetic means aiming to achieve full-thickness and uniform HAp deposition in hydrogel for bone defect repair.

1. Introduction

Reconstruction of bone defects caused by trauma, tumors, infections, has historically been a challenge for both patients and doctors [1,2]. The clinical treatment for bone defect repair primarily includes autografts, allografts, and artificial bone scaffolds [3]. Autografts, as the "gold standard" for bone reconstruction, pose many advantages such as good osteoconductivity, osteoinductivity, and osteogenic matrix. However, these grafts are generally limited by complications including limited bone mass, donor site damage, and low availability. Allografts are also restricted to possible disease transmission, immunological rejection, and social ethical controversy [4–6]. Consequently, it is particularly significant and challenging to develop an ideal artificial bone graft for bone regeneration.

Collagen (Col), a common type of hydrogel, has been widely utilized as scaffolds in bone repair due to the excellent biocompatibility and easy modification [7]. The poor mechanical properties limit Col applications in bone repair [8]. Although several strategies have been attempted to reinforce their mechanical strength, satisfactory strength for bone regeneration was still unachieved [9]. Emerging evidence has confirmed that graphene oxide (GO) is acknowledged as a promising nanomaterial to improve the mechanical properties of hydrogels [10,11]. Of particular, abundant functional groups, such as hydroxyl and carboxyl groups on GO, are beneficial to form chemical bonds with hydrogels. Furthermore, the π-π bonds on the GO can adsorb proteins and ions to enhance stem cell proliferation and differentiation [12,13]. Nevertheless, the practical application of these GO-based hydrogel is still confronted with compromised osteoconductivity.

Nowadays, the hydroxyapatite (HAp), which is produced by biomimetic mineralization process using simulated body fluids (SBFs), has become the most popular bone substitute material attributing to the similarity in the inorganic component of human and animal bones, good biocompatibility, osteoconductivity, and osteoinductivity [4,14–16]. The crystalline structure and morphology of HAp play vital roles in mediating cellular behaviors [17–20]. For instance, the crystalline structure of HAp affects the release process of Ca and P ions, which regulate the cell fate

* Corresponding author.
** Corresponding author.
E-mail addresses: Sunjm1592@sina.com (J. Sun), benjamin.wzx@163.com (Z. Wang).

[19]. The morphology of HAp can provide biophysical information for adjusting cell behaviors [18]. In addition, the roughness surfaces of HAp can facilitate cell adhesion and proliferation [20]. Unfortunately, HAp formed by SBFs is often poorly distributed in the central area of some large stents or three-dimensional (3D) complex stents. Although the porous structure can increase the HAP deposition depth to a certain extent, the low perfusion efficiency in the central area of the stent and the spatial occupying effect of the deposited HAP make it still difficult to achieve full-layer mineralization [21]. The lack of HAp in the depth of the stents can't effectively release ions and promote the cell growth into the stents which limits its clinical application [22,23].

The studies learning from natural pearls, pearls, bones, bamboo, teeth, have provided countless inspiration for solving the problem of bone defects [24–26]. Pearl, consisting of calcium carbonate platelets and organic matrix, exhibits high strength, and uniform mineralization, which were mainly attributed to the hierarchical "brick-and-mortar" layered architectures [27,28]. In addition, the pearl-inspired artificial materials is able to easily adjust the compositions of the materials to acquire the desired properties [29,30]. However, most pearl-inspired materials lack satisfying pore size and breathability, which are important properties for hydrogels to recruit cells and nutrients from the surrounding environment for tissue regeneration [31–35].

Based on the above reports, in this work, the pearl-inspired microgels were successfully well-constructed using GO and Col as building blocks in combination with HAp-based uniform mineralization. Specifically, we prepared the multi-layer mineralized GO-Col-HAp (MMGCH) microgels by the microarray chip and multiple encapsulation to obtain the multi-layered structure. Followed by mineralizing in SBFs to develop uniform distributed HAp (Fig. 1). Here, systematic in vitro experiments were performed to estimate porous and uniform HAp distribution in the microgel as well as to evaluate the impact of the microgel on cell proliferation and osteogenic differentiation. Furthermore, we also adopted the in vivo validation to explore its ability to regenerate bone tissues in rat calvarial and mandibular defect model. Based on these results, we here demonstrated the feasibility of generated uniformly distributed HAp microgels for the potential application of bone regeneration and biomimetic construction.

2. Experimental section

2.1. Materials and animals

Graphene (500 meshes) was purchased from Acros Organic Company (USA). N-(3-Dimethylaminopropyl)-N-ethylcarbodiimide hydrochloride crystalline (EDC), N-hydroxysuccinimide (NHS), and Collagen (Type I, from bovine skin) were purchased from Sigma-Aldrich (USA). All chemicals were used as received.

All animals were purchased from the Department of Experimental Animals, Tongji Medical College, Huazhong University of Science & Technology (Wuhan, China). The experimental protocol was formally approved by the Department of Experimental Animals, Tongji Medical College, Huazhong University of Science & Technology (Wuhan, China).
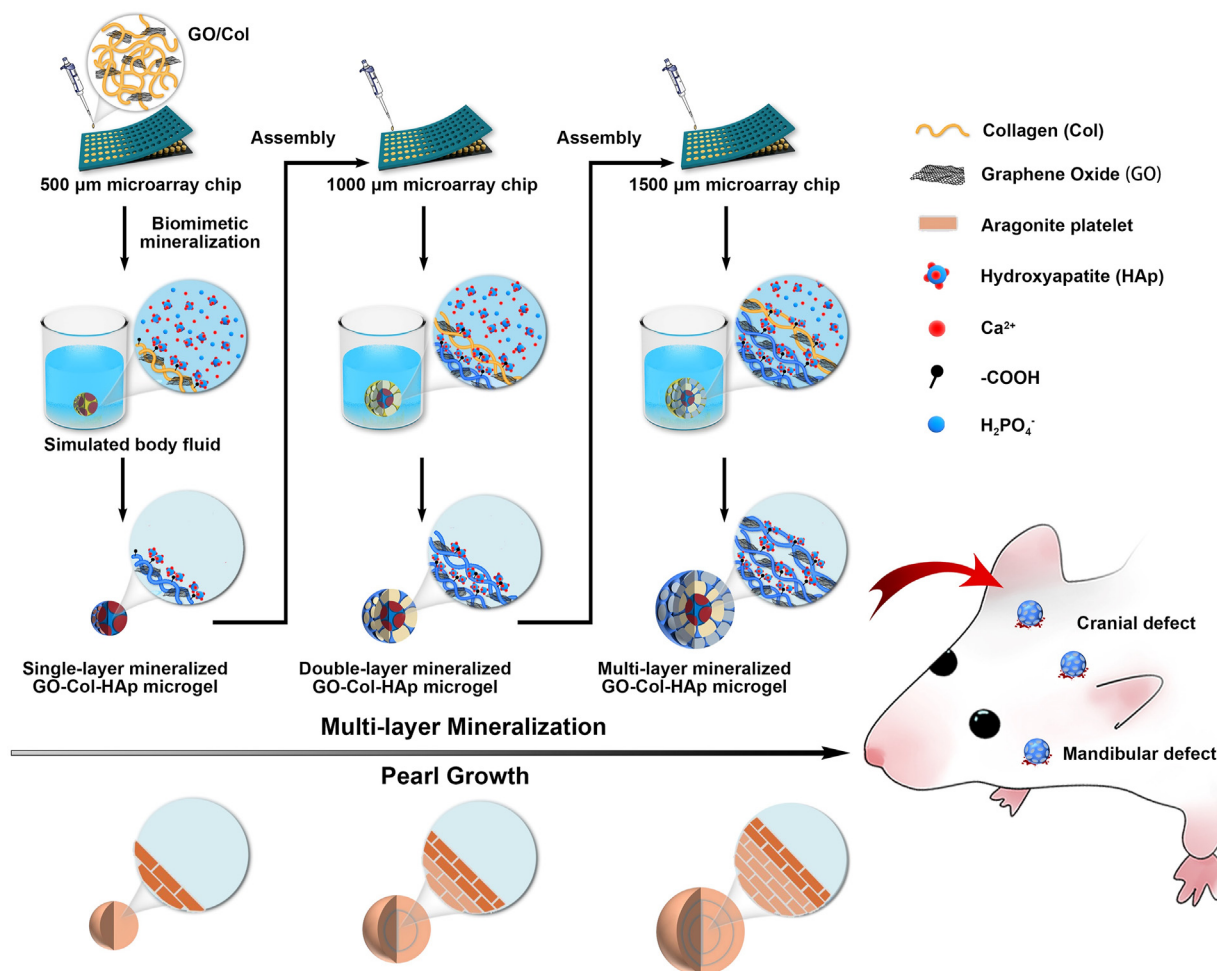

Fig. 1. Schematic illustration of the preparation of multi-layer mineralized GO-Col-HAp microgels with uniform HAp deposition and their applications in rat cranial defect and mandibular defect repair.

2.2. Fabrication of microgel

Graphene oxide (GO) was prepared using a modified Hummer method as previously reported [36]. The micro-stencil array chip using polymethyl methacrylate (PMMA) was fabricated by laser prototyping technique according to our previous report [37]. The MMGCH microgels were synthesized by chemical crosslinking and biomimetic mineralization, as illustrated in Fig. 1. Briefly, a certain amount of mixed GO/Col solution (0.1% w/v GO and 2% w/v Col in 0.1 M HAc) was transferred to the micro-stencil array chip (261 circle wells with a 500 μm diameter) and scraped back and forth to ensure uniform distribution, followed by freezing overnight at $-20\ °C$ and subsequently lyophilizing for 24 h at $-50\ °C$ under vacuum. The 500 μmφ microgels were removed from the chip and immersed in 95% ethanol. To crosslink GO and Col, EDC and NHS were added to ethanol and stored at room temperature for 24 h. Then, the obtained microgels were washed with ddH$_2$O for 3 times and lyophilized in vacuum at $-50\ °C$ for 24 h to remove the by-products. Once the microgels were lyophilized, the microgels were immersed with CaCl$_2$ and K$_2$HPO$_4$ solution to obtain nucleation sites for the next bionic mineralization in simulated body fluids (SBF), as described above [5]. In brief, the microgels were immersed in 20 mL CaCl$_2$ solution (0.444g, 0.2 mol/L) for 3 min and 20 mL of ddH$_2$O for 10 s, followed by immersing in 20 mL K$_2$HPO$_4$ (0.696g, 0.2 mol/L) for 3 min and 20 mL of ddH$_2$O for another 10 s. The entire process was repeated three times. Then, the microgels were immersed into SBF for 7 d and lyophilized again. To cover the second layer around 500 μmφ microgel, GO/Col solution was pipetted onto the micro-stencil array chip (261 circle wells with a 1000 μm diameter), and then inserted 500 μmφ microgels into each well. The 1000 μmφ mineralized microgels were obtained by repeated chemical cross-linking and biomimetic mineralization. To cover the third layer around 1000 μmφ microgel, GO/Col solution was pipetted onto the micro-stencil array chip (261 circle wells with a 1500 μm diameter). Then, the 1000 μmφ mineralized microgels were put into each well. Finally, the multilayer (three layer) MMGCH microgels were manufactured by repeated chemical cross-linking and bionic mineralization. In the same way, the multilayer MGC microgels were fabricated by multiple encapsulation of the microgels (with three sizes: 500 μm, 1000 μm, and 1500 μm) without mineralization. The multilayer SMGCH microgels were fabricated by mineralizing the MGC microgels in SBF for 7 d and lyophilized. In the following experiments, the microgels were used in the form of dry scaffolds in physiochemical evaluations and in the form of wet hydrogels in cellular and bone regeneration evaluations.

2.3. Characterization of microgel

The surface, coronal-section, and cross-section morphologies were characterized using field emission scanning electron microscopy (FSEM; GeminiSEM300, German) at 10 kV. The Ca/P ratio and distribution of bionic apatite were evaluated by energy dispersive spectroscopy (EDS). X-ray diffractometer (XRD; Empyrean, PANalytical B.V.) was used to evaluate crystalline phases of the microgels at a scanning rate of 0.013 $°s^{-1}$ in a 2θ range from 5° to 40° with CuKα radiation (k = 1.540598 nm). FTIR spectroscopy (VERTEX 70; Bruker company, German) was applied to evaluate functional groups of the microgels from 4000 cm^{-1} to 500 cm^{-1} at a resolution of 0.4 cm^{-1}. TGA was used to calculate apatites content in the microgels at a heating rate of 10 °C/min from 25 °C to 800 °C in the N$_2$ atmosphere. The modulus of microgels was estimated by All-Electric Dynamic Test Instrument (ElectroPuls E1000, INSTRON, British) at a loading rate of 1 mm/min until the 80% compression of microgels was reached. The amplitude sweep test was performed at a fixed frequency of 1Hz in the range of 0.01–100% to investigate the rheological change related to shear strain. The porosity of microgels and pearl was measured by the liquid displacement method [11]. The dry samples were weithged (W$_0$) and immersed in water for 12 h. These wet samples were weithged (W$_1$) again. The porosity was obtained by the equation:

$$Porosity(\%) = [(W_1 - W_0) / \pi \rho h(d/2)] \times 100\%$$

ρ values 1.00 mg/mm^3, π values 3.14159, d and h are the diameter and thickness of the samples separately.

The mass of the microgels was measured using an electronic analytical balance (accurate to 10^{-5} g). The mass increase of the microgels before and after the mineralization was calculated. Microgels were immersed in 0.5 m acetic acid overnight to dissolve mineralized apatites. Then, the calcium assay kit (Jiancheng, Nanjing, China) was used to calculate the calcium content according to the manufacturer's instructions.

The swelling test was performed to investigate the swelling ratio (SR) and stability of the microgels. The freezy-dried microgels were put into 10 mL PBS (0.01 M, Ph 7.4) in sealed vials at 37 °C. Then, the microgels were taken out from the solution and weighed at scheduled time points (0, 3, 6, 12, 24, 36, 48 h). The SR was calculated using the equation:

$$SR(\%) = (W_t - W_0)/W_0 \times 100\%$$

W$_t$ represented the weight after swelling, W$_0$ represented the initial weight.

For the degradation test, all of the microgels were incubated in 20 mL collagenase solution (20 unit/mL) at 37 °C, respectively. Then, the microgels were taken out from the solution and washed with ddH2O three times at scheduled time points (0, 10, 20, 30 days). Followed by freezy-drying and weighting. The degradation (%) was calculated using the equation:

$$Degradation\ rate\ \ (\%) = (W_0 - W_t)/W_0 \times 100\%$$

W$_t$ and W$_0$ represented the dry weight of the microgels after degradation at scheduled time points and the dry weight of the initial microgels, respectively.

2.4. Isolation, culture, and seeding of rat BMSCs

Rat BMSCs (r-BMSCs) were isolated as described previously [38]. For in vitro culture, the r-BMSCs were grown in low glucose Dulbecco's Modified Eagle's Medium (DMEM, HyClone, USA) supplemented with 10% fetal bovine serum (FBS, HyClone, USA), 1% penicillin and streptomycin (Thermo Fisher Scientific, USA). Prior to cell seeding, the microgels were sterilized by immersing in 75% ethanol for 30 min, washed with PBS for 3 times, and soaked in DMEM overnight. The r-BMSCs (passage 3) were digested with trypsin and re-suspended at a density of 5×10^6 cells/mL. Then, 20 sterilized microgels were placed in a 6-well plate (Corning) and were seeded with 60 μL of cell suspension. After incubation for 2 h, the cell-seeded microgels were transferred to a new 6-well plate and cultured in 2 mL DMEM. The cultures were maintained in an incubator at 37 °C in 5% CO$_2$, and the media were replaced every 3 days.

2.5. In vitro evaluation of the microgel on cell proliferation

Living cells were represented by fluorescein diacetate (FDA, Sigma) and dead cells were represented by propidium iodide (PI). In brief, the cell-seeded microgels at corresponding time points (1, 4, and 7 d) were washed with PBS for 3times , then 2 mL FDA (2 μg/mL) was added to a 6-well plate. After incubation at 37 °C for 30 min in darkness, the microgels were washed with PBS, then, 2 mL PI (100 μg/mL) was added to a 6-well plate. After dark incubation at room temperature for 10 min, the microgels were washed with PBS and observed under confocal laser microscope (Leica Microsystems, Wetzlar, Germany) (n = 3 for each time point). The cell-seeded microgels at day 7 were washed with PBS for 3 times and fixed with 2.5% glutaraldehyde for 3 h. After PBS washing, the microgels were dehydrated by applying serial concentrations of ethanol (50%, 75%, 80%, 90%, and 100%). After air-drying and sputtering with gold, the microgels were observed by FSEM.

The cell-seeded microgels at indicated time points (1, 3, and 7 d) were

transferred in a 96-well plate. Then, 50 μL MTT (5 mg/mL in PBS, Sigma, St. Louis, USA) and 100 μL growth medium were added in 96-well for 4 h incubation at 37 °C in 5% CO_2 in darkness. Next, the microgels were washed with PBS and treated with 150 μL dimethyl sulfoxide (DMSO, Sigma, USA). Subsequently, DU 730 UV/Vis spectrophotometer (Beckman Coulter, USA) was applied to record absorbance at 570 nm wavelength.

2.6. In vitro evaluation of the microgel on cell osteogenic differentiation

The r-BMSCs were seeded on microgels cultured for 4 d and 7 d of osteoinductive culture and then the total protein of r-BMSCs was extracted from the microgels. A total of 40 μg protein were loaded onto 10% SDS/PAGE gel and then transferred to PVDF membrane (Millipore, USA). After blocking, the pre-treated PVDF membranes were incubated with rabbit ALP, OCN, COL-1 polyclonal antibodies (Abcam, USA), and GAPDH monoclonal antibody (Sigma, USA), respectively at 4 °C overnight. Then the bands were incubated with horseradish peroxidase (HRP)-conjugated secondary antibodies at room temperature for 2 h. The targeted proteins were visualized using ECL reagents and quantified using image j software. qRT-PCR was used to analyze osteogenesis-differentiation of r-BMSCs cultured on/in microgels for 4 d and 7 d. The targeted miRNAs were alkaline phosphatase (ALP), osteocalcin (OCN), and collagen type-1 (COL-1), while glyceraldehyde 3-phosphate dehydrogenase (GAPDH) was used as an internal control for mRNAs. The primer sequences were listed in Supporting Information Table S1. Immunohistochemical staining kit (Abcam, UK), osteocalcin (Abcam, UK) in cells on/in microgels were observed under the fluorescent microscope. The osteoinductive cultured microgels for 7 d were fixed with 4% paraformaldehyde for 30 min and then permeated with 0.1% Triton X-100 for 15 min. Then, the processed sections were blocked with diluted ghost serum antibody for 30 min, and then incubated with OCN monoclonal antibody separately.

2.7. Cranial and mandibular defect orthotopic bone formation in rat

For cranial defect orthotopic bone formation, SD rats were anesthetized using inhaled isoflurane and subcutaneous buprenorphine injection. The sagittal incision with 2 cm length was cut on the middle of the scalp in each rat. After cleaning the fascia and showing skull bone, two parallel 5 mm critical cranial defects were drilled. The microgels was then inserted into the defect area to close the incision (n = 8/group). Right mandibular incision was performed to induce in situ bone formation of mandibular defect. Then, muscle and fascia were cut open to expose the mandible. A severe mandibular defect of 5 mm was then drilled and microgels were finally inserted into the defect area to close the incision (n = 16/group). Implanted specimens were harvested at week 4 and 12 post-operation. Micro-CT scanner (SkyScan 1176; Broker) was used to assess new bone formation. Bone volume/tissue volume (BV/TV), and bone mineral density (BMD) were calculated using CTAn software.

2.8. Histology and immunohistochemical staining

Before staining, the harvested samples at indicated time points (4 and 12 w) were fixed with formalin for 7 days and then decalcified in 10% Ethylene Diamine Tetraacetic Acid (EDTA) for 4 weeks. Then, the samples were embedded in paraffin and sectioned to 3 μm pieces at the mid-sagittal plane of the defect area. The sectioned samples were stained with HE and Masson's Trichrome (Sigma, USA), and observed under the microscope (Eclipse Ni-E; Tokyo, Japan). The processed sections were blocked by diluted ghost serum antibody for 30 min, followed by incubating with COL-1 and OCN monoclonal antibodies (Abcam, UK) separately. Finally, the staining samples were observed under microscope.

2.9. Statistical analysis

All data presented in the experiments were expressed as mean ± standard deviation (SD). The statistical differences ($p < 0.05$) were measured by student's t-test for two groups comparing, and one-way analysis of variance (ANOVA) containing post hoc contrasts by Student-Newman-Keuls test or Kruskal-Wallis nonparametric procedure followed by Mann-Whitney *U* test for multiple-groups comparing.

3. Results

3.1. Fabrication of the multi-layer mineralized and porous microgels

The fabrication process of multi-layer mineralized GO-Col-HAp microgels (MMGCH) was shown in Fig. 2. According to our previous study, the optimum GO concentration was 0.1% w/v and optimum mineralization time in SBF was 7 d [5]. Hence, 0.1% w/v GO/Col solution was fabricated and pipetted into the micro-stencil array chip. EDC and NHS were used as crosslinking reagents to form amide bonds between Col and GO, and biomimetic mineralization was carried out for 7 days followed by multiple encapsulation to develop MMGCH microgels (Fig. 2A). The scheme and optical images of these 3 types of microgels (Fig. 2B) and pearl (Fig. 2C) were exhibited. Hydroxyapatite coating made the surface of SMGCH and MMGCH microgels appear white. The microgels were immersed in water and the multi-layer structure and pore structure could be observed under the microscope (red arrowheads) (Fig. 2B, S1A).

The porosity of the microgels and pearl (MGC: 82.3 ± 5.5%, SMGCH: 85.3 ± 6.8%, MMGCH: 84.4 ± 10.6%, pearl: 0%) was calculated and no differences were observed between microgel groups (Fig. 2D). To observe the HAp deposition in the microgels and pearls, micro-CT was used to analyze the 3D reconstructed images. The results showed that HAp was uniformly distributed in the MMGCH group and the pearl group, while the dense sphere with no pore structure was reconstructed in the pearl group. The analysis of apatite volume/total volume (Fig. 2E) and apatite mineral density (Fig. 2F) exhibited that there was more HAp mineralization in the MMGCH group compared to SMGCH and MGC groups. The layered structure can be observed when the pearl is broken open (Fig. S2A), and the "brick-and-motar" architecture can be observed in the SEM images (Fig. S2B).

3.2. Morphology and physiochemical evaluation of the microgels

In this study, the porous structures were observed among these surface, coronal-section, and cross-section of the microgels in SEM images (Fig. 3A). The porous structure was mainly devoted by evaporation of solvent in the microgels through vacuum drying method to develop a pore structure and then connecting with each pore to form an interconnected structure. The pore size of these microgels varied from 80 μm to 150 μm (Fig. 3F), which could guarantee desirable cell infiltration and nutrient exchange inside the microgels [39,40]. Intrestingly, with the growth of HAp crystals on the superficial of the microgels, the pore sizes gradually decreased (Fig. S3). Moreover, After swelling, the porous and interconnected structures did not change significantly compared with that before swelling, which indicated the good structural stability of the microgels. While the pore sizes of the MGC, SMGCH, and MMGCH microgels increased to 243.0 μm ± 21.1 μm, 212.0 μm ± 16.5 μm, and 224.7 μm ± 13.5 μm (Fig. S4). Furthermore, multi-layered structures (red for inner layer, yellow for middle layer, and blue for outer layer) could be observed both in the coronal-section and cross-section (Fig. 3A). HAp, represented by white arrowheads, was uniformly distributed on the surface, coronal-section, and cross-section of the MMGCH group. The uniform distribution of HAp in the MMGCH group could also be further confirmed by energy dispersive X-ray spectrometers (EDS) mapping and EDS point evaluations. The Ca and P mapping of HAp were bright and uniformly distributed in the interface regions of microgels. The Ca/P
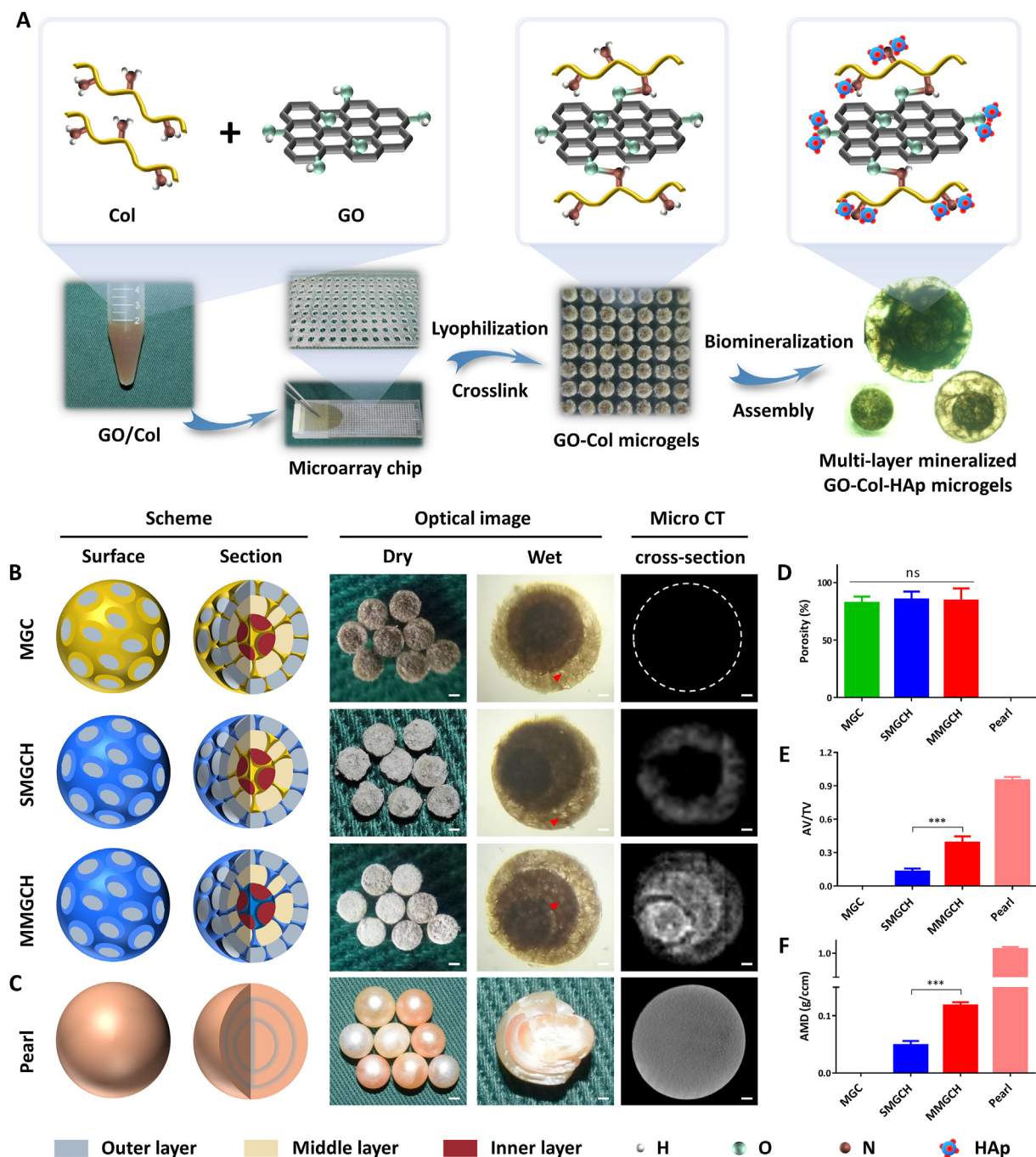
Fig. 2. Fabrication of multi-layer mineralized GO-Col-HAp microgels and their schematic illustrations. (A) Experimental steps for the synthesis of multi-layer mineralized GO-Col-HAp microgels using microarray chip and their chemical reaction illustration. (B) Schematic drawing, optical image, and micro ct evaluation of the microgels (Scale bars of low magnification: 500 μm, scale bars of high magnification and micro ct: 200 μm, red arrowheads refer to pore structure). (C) Schematic illustration, optical image, and micro ct analysis of the pearl (Scale bars of low magnification: 5 mm, scale bars of high magnification and micro ct: 1 mm). (D) The porosity of the microgels and peral. (E–F) Quantitative analysis of apatite volume to total volume (AV/TV) and apatite mineral density (AMD) of microgels and pearl (ns: no significance, ***p < 0.001).

ratios of the HAp were indistinguishable with the numbers varied between 1.62 and 1.68 (Fig. 3B).

The chemical structure of microgels was analyzed by infrared spectroscopy (Fig. 3C). The absorption peak at 1646 cm^{-1} indicated the stretching vibrations of amide I, and the peak at 1590 cm^{-1} represented the bending vibrations of amide II. These two absorption peaks demonstrated that the amide bond (–NHCO–) was successfully formed due to the cross linking of GO and Col [38,41]. The characteristic absorption peaks at 1028 cm^{-1} and 961 cm^{-1} were observed in the curve of SMGCH

and MMGCH groups, which corresponded to the (002) and (211) crystalline planes respectively [40]. These diffraction peaks were in good agreement with those of standard HAp (JCPDS No. 74–0566) [42], confirming successful mineralization of HAp in the microgels. The presence of HAp in the microgels can also be evident in XRD measurements (Fig. 3D). The characteristic 26.1° and 31.7° diffraction peaks of HAp were detected in SMGCH and MMGCH groups, which indicated a perfect crystalline structure of HAp in the microgels [43]. To calculate HAp content in the microgels, thermogravimetric analysis (TGA) was
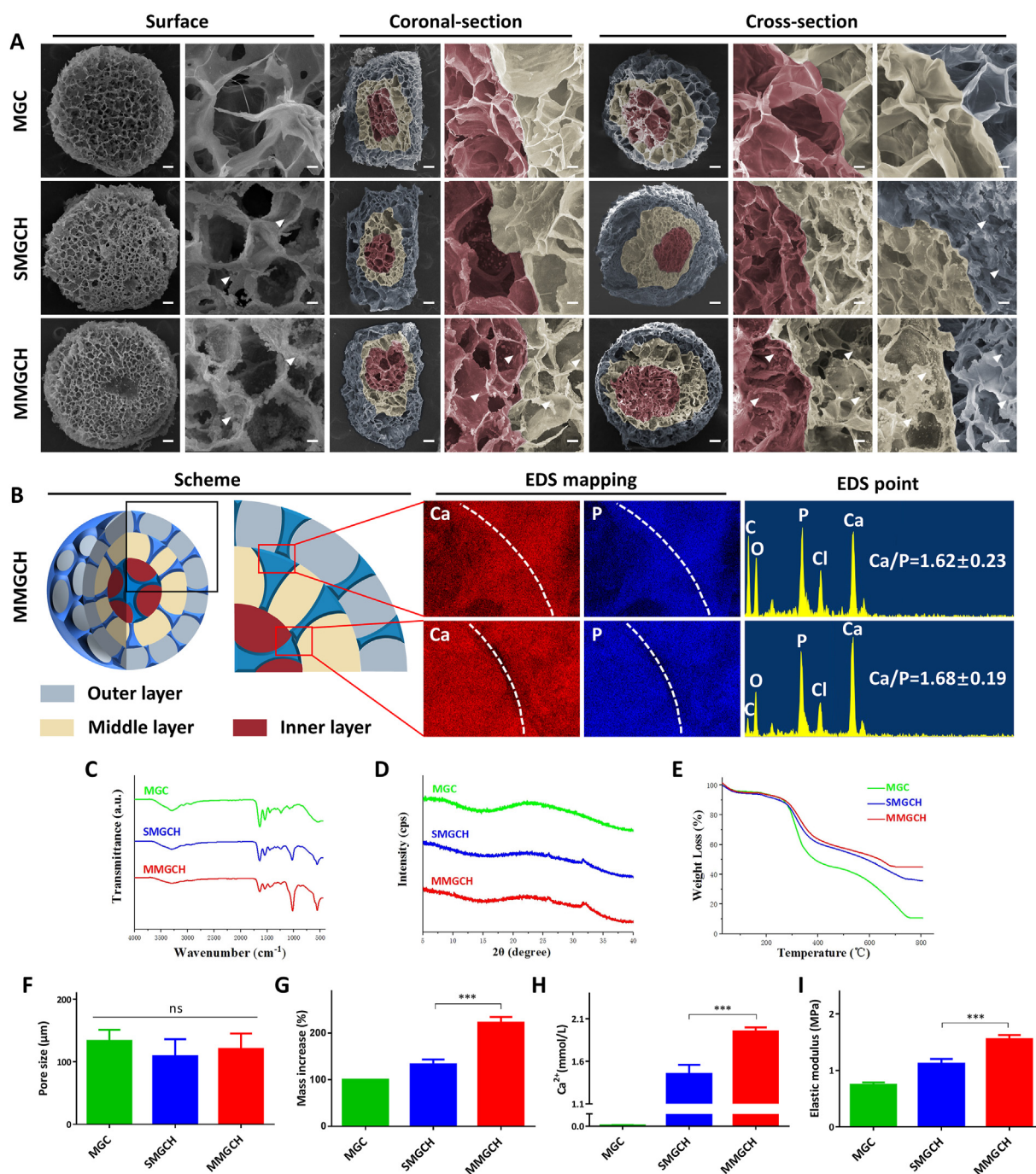
Fig. 3. Morphology and physiochemical evaluation of the microgels. (A) SEM images of the surface, coronal-section, and cross-section morphologies of the microgels (Scale bars in low magnification images were 100 μm, and in high magnification images were 10 μm. The red regions represented for the inner layer, the brown regions represented for the middle layer, the blue regions represented for the outer layer, and the white arrowheads represented for HAp). (B) Schematic illustration and EDS mapping images of Ca and P elements and EDS point images of the MMGCH microgels. (C–E) FTIR spectra, XRD spectra, and TGA analysis of the microgels. (F) Pore size of the microgels. (G) Mass increase of the microgels after biomimetic mineralization in SBF. (H) Calcium quantitative analysis of the microgels. (I) Elastic modulus evaluation of the microgels (ns: no significance, $*p < 0.05$, $**p < 0.01$, $***p < 0.001$).

performed and the weight loss was figured according to the TGA curve of microgels (Fig. 3E). This result showed that the residual weight of MMGCH (46.3%) was higher than that of the SMGCH group (37.2%) and MGC group (10.5%), suggesting that there was more HAp in the MMGCH group. Furthermore, the weight increase rate was calculated according to the weight change during the mineralization process, and HAp content in the microgels was analyzed (Fig. 3G). Similar results were observed that the MMGCH group showed a higher mass increase ($222.0 \pm 12.6\%$) than the SMGCH group ($133.2 \pm 10.22\%$). From the quantitative experiment

of calcium, MMGCH group also displayed more calcium than the SMGCH group (Fig. 3H).

In addition to the morphology and distribution of HAp in the microgels, the mechanical strength of the hydrogels should also be considered. The elastic modulus of MMGCH (1.95 ± 0.05 MPa) was quite high (Fig. 3I). Moreover, the corresponding compression stress-strain mesurements confirmed the result that MMGCH exhibited high mechanical strength (Fig. S5A). Additionally, the amplitude sweep test was performed from 0.01 to 100% of shear strain at a constant angular

frequency to observe any deformation of the microgels during a change of strain (Fig. S5B). All microgels exhibited higher storage modulus (G') than loss modulus (G"), which was a characteristic of viscoelastic solid. The MMGCH microgels showed higher storage modulus and loss modulus. For shear strains from 0.01% to 10%, all microgels were stable. However, the storage modulus started to decrease as the strain exceeded 10%. Finally, all microgels exhibited reversible deformation as the strain exceed 30%. To exhibit the stability and swelling properties of the microgels, The swelling ratios of the microgels were measured (Fig. S6A-

B). All microgels exhibited high swelling ratios, and the MMGCH microgels showed the highest swelling ratio of 575.63% $\pm$ 11.07% at 48h. Moreover, the degradation rate of the microgels were evaluated. all of the microgels were incubated in collagenase solution (20 unit/mL), respectively (Fig. S6C). The degradation rate increased with the incubated time prolonged. The MGC, SMGCH, and MMGCH showed 42.20% $\pm$ 1.10%, 48.27% $\pm$ 1.05%, and 50.53% $\pm$ 1.11% on day 30.
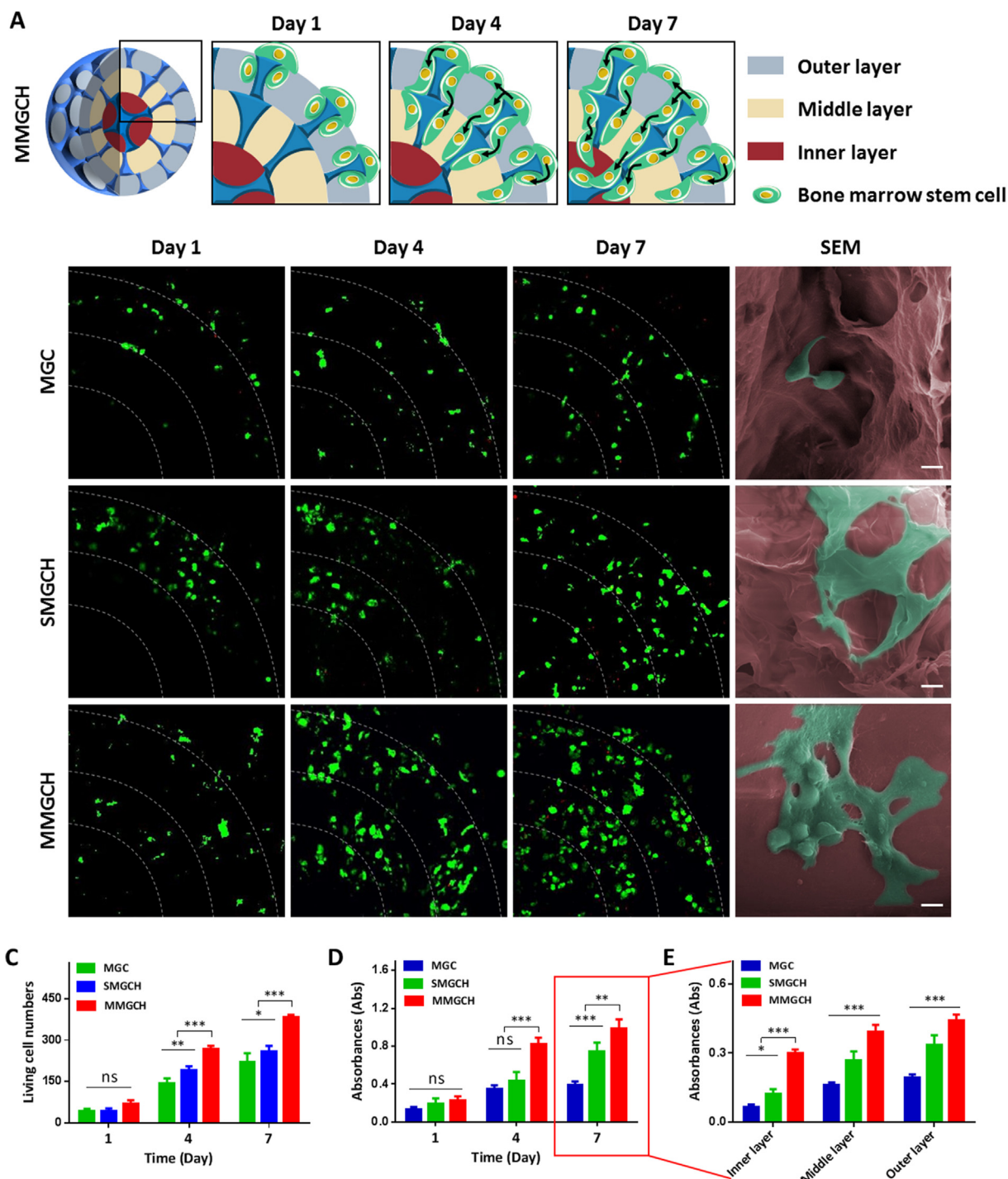

Fig. 4. In vitro evaluation of migration and proliferation of r-BMSCs on/in the microgels. (A) Schematic illustration of cell migration and proliferation on/in the microgels. (B) Live/dead staining and SEM images of r-BMSCs on/in the microgels (Scale bars in confocal images: 100 μm, and scale bars in SEM images: 10 μm). (C) Quantitative analysis of living cells on/in the microgels at day 1, 4, and 7 post-incubation. (D) Cell viability of r-BMSCs on/in microgels at day 1, 4, and 7 post-incubation. (E) Quantitative analysis of fluorescence intensity in different layers measured at day 7. (*p < 0.05, ***p < 0.001, ns: no significance).

3.3. Analysis of the microgels on cell migration and proliferation

To verify the hypothesis that the pearl-inspired microgels can provide a stable cellular environment, we first investigated the cell migration of r-BMSCs in the microgels by using live/dead staining. In schematic illustration, the r-BMSCs (in green) were mainly distributed in the outer layer of microgels at day 1, and continuously migrated into the inner layer at 7 d (Fig. 4A). High fluorescence intensity of stained living cells was observed in the MMGCH group both at day 4 and day 7. Furthermore, the morphologies of r-BMSCs at the inner layer of the microgels were examined by SEM after culturing for 7 d (Fig. 4B). Stretched and extended r-BMSCs (in green) were observed in the SMGCH and MMGCH group while clustered cells were attached in MGC group. In addition, more cells were observed in the MMGCH group. The living cell numbers of r-BMSCs were quantitatively studied after 1, 4, and 7 d culture with microgels. The living cell numbers varied with time in the three groups, and the number in the MMGCH group was higher than the other two groups (Fig. 4C). Similar results were observed using the MTT assay. After incubating r-BMSCs for 1, 4, and 7 d in the microgels, the MMGCH group exhibited higher fluorescence intensity, meaning that higher cell viability in the microgels (Fig. 4D). Particularly, significant higher

fluorescence intensity was observed in the inner region of the MMGCH group at day 7 post-incubation (Fig. 4E).

3.4. In vitro evaluation of the microgels on cell osteogenic differentiation

To analyze the effect of the microgels on promoting the osteogenic differentiation of stem cells, the r-BMSCs were seeded on microgels and cultured in osteoinductive medium for 4 d and 7 d (Fig. 5A). The western blot assay showed that there were significant higher protein expression levels of alkaline phosphatase (ALP), osteocalcin (OCN), and collagen type-1 (COL-1) in the MMGCH group (Fig. 5B–C). It was consistent that qRT-PCR confirmed that the osteogenic gene levels of ALP, OCN, and COL-1 were up-regulated in the MMGCH group at day 4 and day 7 after osteogenic induction, whereas only a slight increase or no obvious change presented in the SMGCH group (Fig. 5D). To evaluate the impact of uniformly mineralized HAp on the differentiation of r-BMSCs, the expression of OCN was immunohistochemically stained and examined after 4 and 7 days of osteogenic incubation. OCN expression (red arrowheads: positive brown staining) was observed in the outer layer among three groups, corresponding to regions of differentiated osteoblasts from r-BMSCs. In contrast, high-expression of OCN was only found
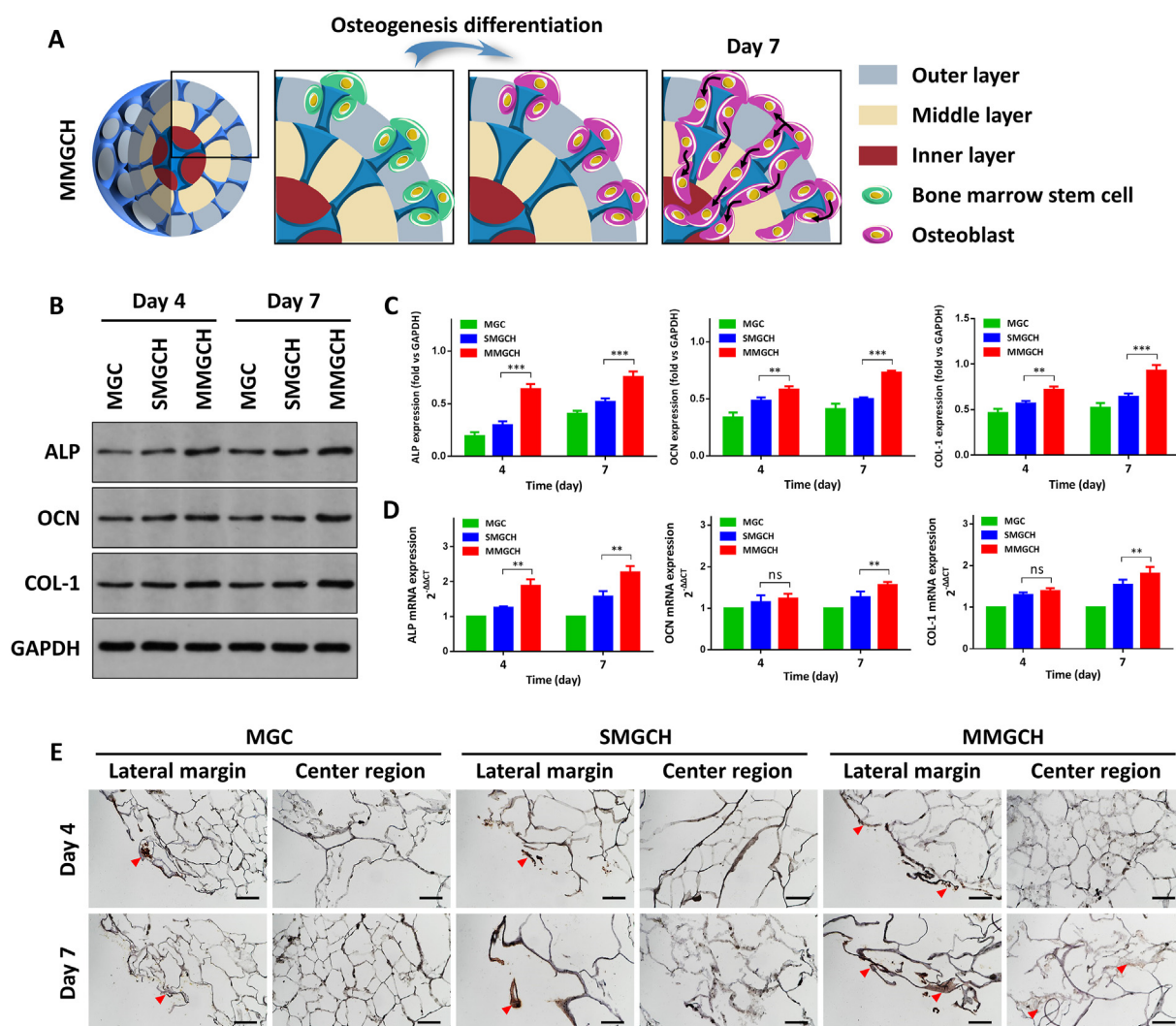

Fig. 5. In vitro evaluation of r-BMSCs osteogenic differentiation on/in the microgels. (A) Schematic illustration of cell osteogenic differentiation on/in the microgels after 4 and 7 days of osteogenic incubation. (B) The protein expression of osteogenic markers of r-BMSCs. (C) Quantitative analysis of ALP, OCN, and COL-1 protein expression for 4 and 7 days on/in microgels, normalized to GAPDH. (D) qRT-PCR analysis of ALP, OCN, and COL-1 gene expression of r-BMSCs during 4 and 7 days of osteogenic incubation respectively. (E) OCN staining of microgels at day 4, 7 post-osteogenic incubation (red arrowheads: positive brown staining, scale bars: 100 μm, ns: no significance, **P < 0.01, ***P < 0.001).

in the inner layer of the MMGCH group (Fig. 5E). Additionally, the quantitative analysis of the positive expression of the OCN confirmed this result (Fig. S7).

3.5. In vivo analysis of cranial and mandibular bone regeneration by microgels

To investigate the osteogenic potential of the microgels in vivo, we established the model of rat cranial bone defects and mandibular bone defects to evaluate the new bone-forming capacities of MGC, SMGCH, and MMGCH groups. These microgels were transferred into 5 mm

critical-sized bone defects (Fig. 6E, H), and the 3D reconstruction images of newly formed bones were analyzed using micro-CT at week 4 and 12 post-implantation (Fig. 6A–D). The newly formed bones were observed to grow from the margins of the defects in all groups, and a fraction of new bone formations were observed in the center region of the defects in the SMGCH group and MMGCH group at week 4 post-implantation (Fig. 6A, C). After 12 weeks of implantation, the cranial bone defects in the MMGCH group were almost fully filled with newly formed dense bone tissue (Fig. 6B). The mandibular bone defects in the MMGCH group also exhibited more bone tissues than the other two groups (Fig. 6D). Quantitative analysis using micro-CT confirmed the results that the MMGCH
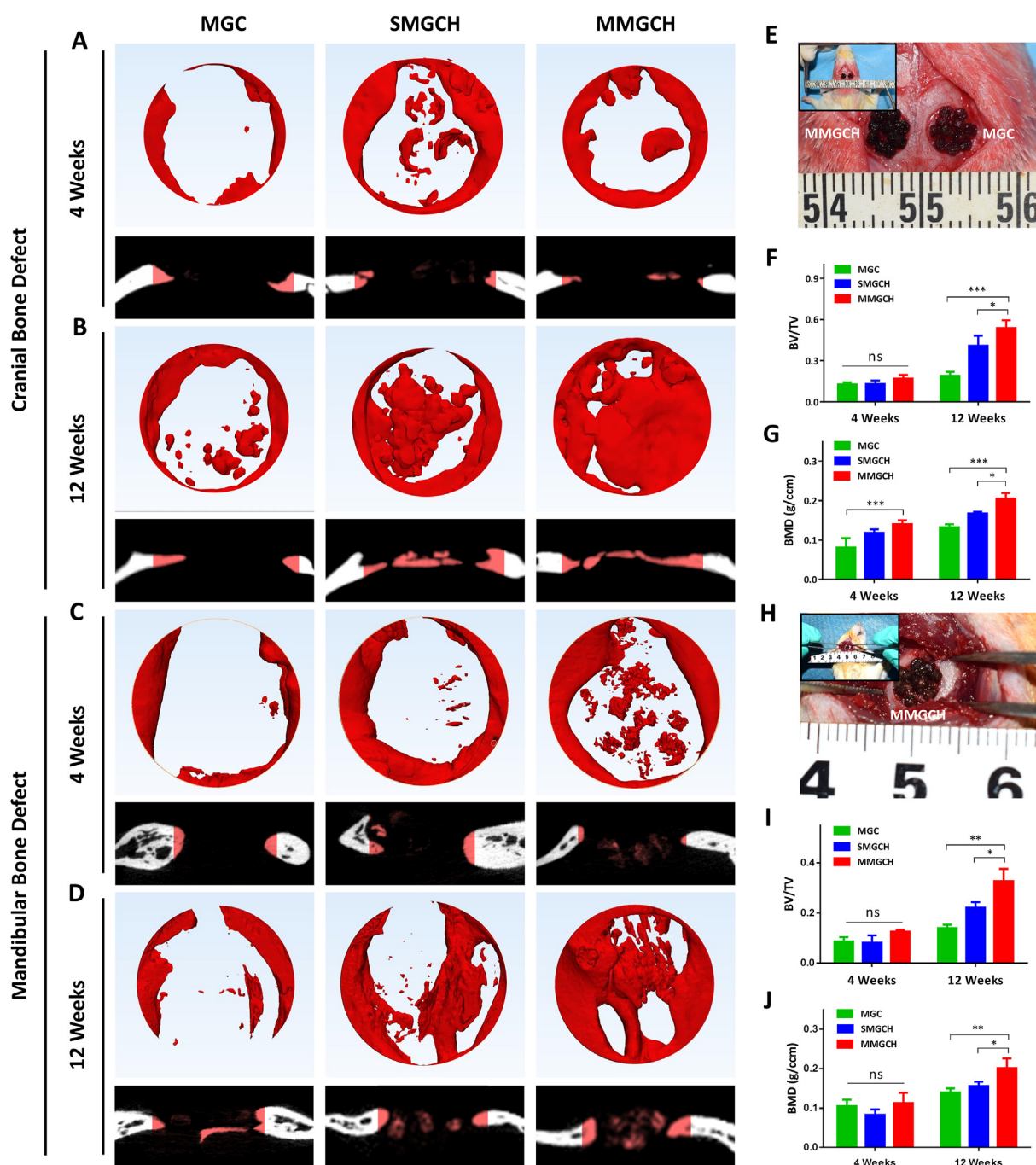

Fig. 6. In vivo evaluation of the microgels for critical-sized cranial and mandibular defect treatment in rat. (A–D) Representative 3D reconstruction and cross-section images of cranial and mandibular bone defects at week 4 and 12 post-implantation. (E, H) Optical images of the microgels in the defect regions during operation. (F–G) Quantitative evaluation of bone volume to tissue volume (BV/TV) and bone mineral density (BMD) in cranial bone defects. (I–J) Quantitative evaluation of BV/TV and BMD in mandibular bone defects. (ns: no significance, $*P < 0.05$, $***P < 0.001$).

group showed significant higher ratios of new bone volume to tissue volume (BV/TV) (Fig. 6F, I) and bone mineral density (BMD) (Fig. 6G, J) both in cranial bone defects and mandibular bone defects at week 12 post-implantation.

Hematoxylin and eosin (HE), Masson's trichrome, and immunohistochemical staining were used to evaluate the bone formation. The morphologies of microgels and newly formed bone tissues were visualized by HE staining (Fig. 7A). At week 4 after implantation, no obvious fibrous membranes and inflammatory response were observed in the large images of HE staining. The microgels in the SMGCH group and the

MMGCH group exhibited a good 3D structure and attracted part of new bone formation at the bottom of the microgels, while the compressed and disorganized structure were found in the microgels of the MGC group (Fig. 7B). After 12 weeks of implantation, a large number of mature and dense bone tissues were observed both in the lateral margin and the center region (white rectangles) in Fig. 7A in SMGCH and MMGCH groups. Furthermore, the defects in the MMGCH group exhibited complete bridging and fully filling of dense bone tissue (Fig. 7B). Masson staining was used to analyze the formation of type I collagen (stained blue) [44]. Similar results were observed that the defect regions in the
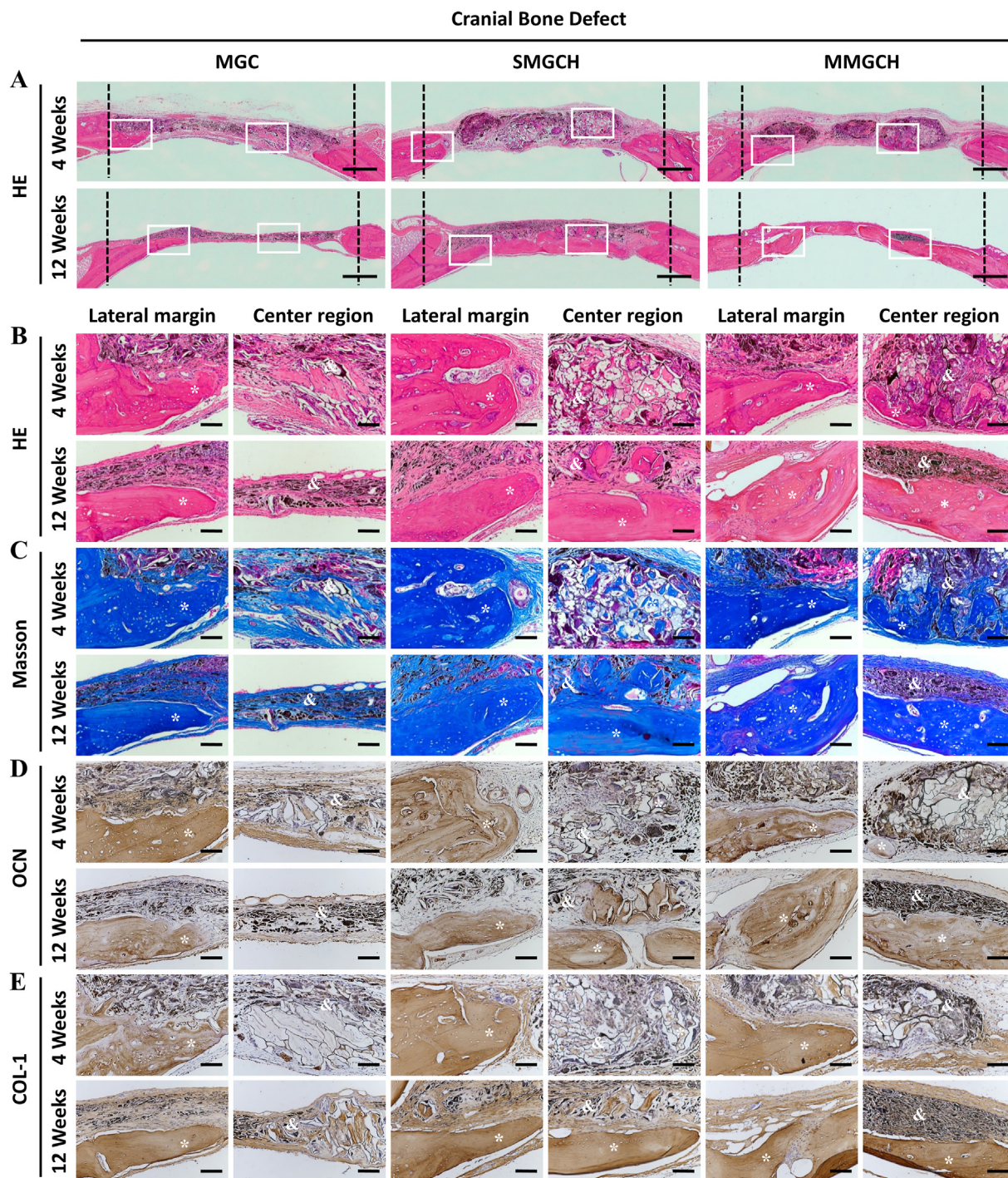

Fig. 7. Histological and immunohistochemical analysis of microgels after implantation for 4 and 12 weeks in cranial bone defects. (A) HE staining images of microgels complexes (Scale bars: 500 μm, white rectangle: the lateral margin and the center region of the defects). (B–E) HE staining (B), Masson's trichrome staining (C), OCN staining (D), and COL-1 staining (E) images of the microgels complexes engineered bone constructs (Scale bars: 100 μm, *: new bone, &: microgels).

MMGCH group were filled with more mature and dense bone tissues than the other two groups (Fig. 7C, **S8A).** For further analysis of the osteogenic potential of the microgels, the expressions of OCN and COL-1 were immunohistochemically stained and evaluated (Fig. 7D–E, **S8B–C)**. The positive expression of OCN and COL-1 (stained brown) in the MMGCH group exhibited dense and thick bone regeneration tissues, which were similar to the HE and Masson results.

The mandibular bone regeneration was evaluated by histological staining, which showed that no obvious newly formed bone tissues were found in the microgel of all groups at week 4 post-implantation. At week 12, a large amount of mature organized bone tissues with a similar structure to native bone were found both in the margin and center regions (white rectangles) of the defect in the MMGCH group (Fig. 8A–B). Masson staining also showed the phenomenon that more new bone formation (Fig. 8C, **S9A**) were generated in defect regions treated with MMGCH microgels. Finally, the expressions of OCN and COL-1 in
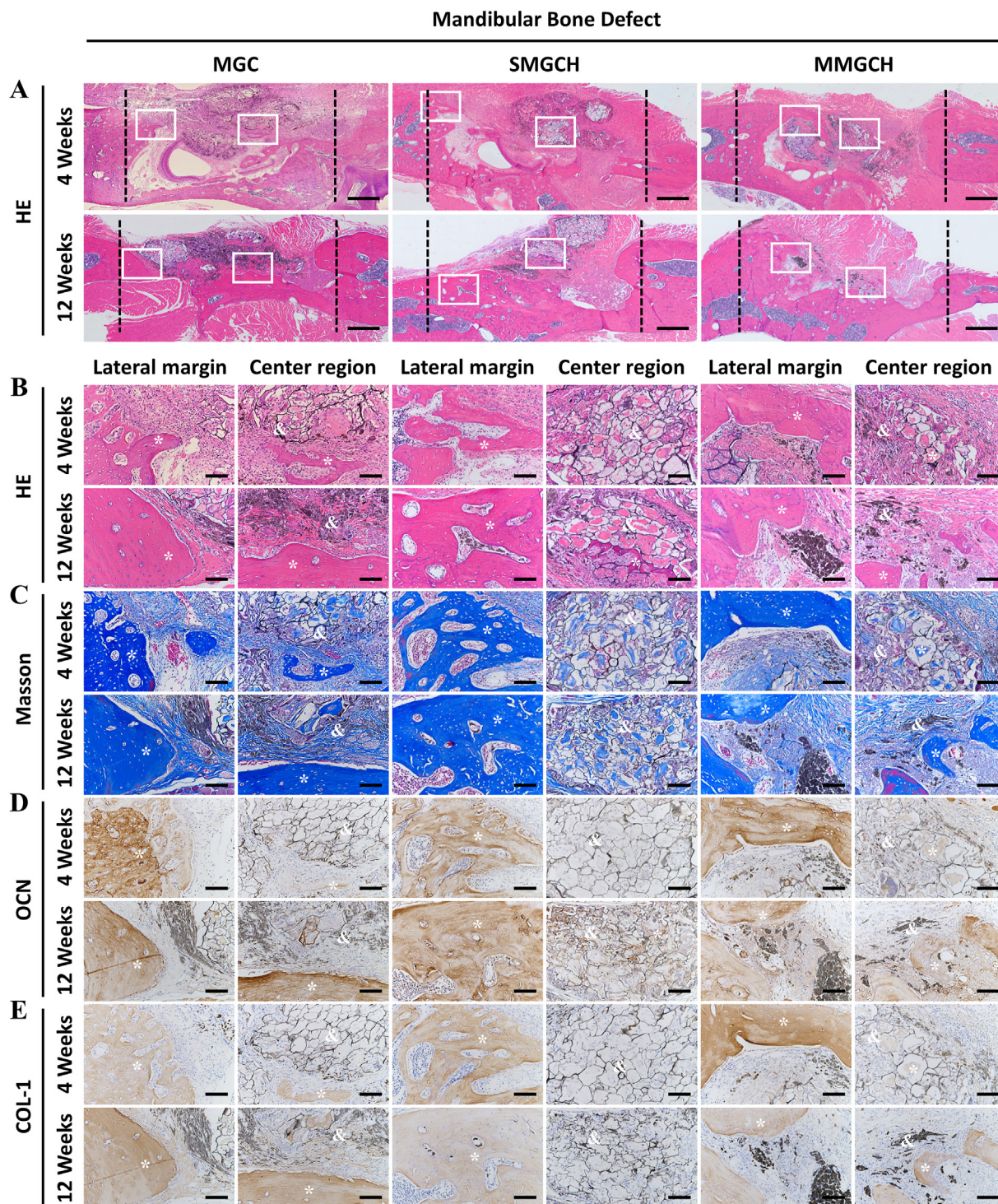

Fig. 8. Histological and immunohistochemical analysis of microgels after 4 and 12 weeks implantation in mandibular bone defects. (A) HE staining images of the defect region at week 4 and 12 pos-timplantation (Scale bars: 500 μm, white rectangle: the lateral margin and the center region of the defects). (B–E) HE staining, Masson's trichrome staining, OCN staining, and COL-1 staining images of lateral margin and center region of the defect region (Scale bars: 100 μm, *: new bone, &: microgels).

osteoblasts were immunohistochemically stained (Fig. 8D–E, **S9B–C)** and evaluated after 4 and 12 weeks of implantation. There were more osteoblasts with high expression of OCN and COL-1 in the MMGCH group.

4. Discussion

Natural pearl provides an optimized guiding principle for the preparation of organized organic-inorganic composite material, where "brick-and-mortar" layered structure provides superior mechanical property and the organic phase contributes to significant bioactivity [29,45]. In the study, we developed the pearl-inspired microgels consisting of multi-layer mineralized Col-GO-HAp hydrogels (500-1000-1500 μm) via the microarray chips molding and the multi-encapsulation assembling procedures. These fabricated microgels exhibited porous structure and suitable mechanical strength. What's more, the pearl-inspired microgels demonstrated time-dependent proliferation and favorable osteogenic differentiation of rBMSCs in vitro. Finally, these microgels possessed satisfactory bone regeneration capacities both in cranial bone defects and mandibular bone defects.

Although biomineralization of natural polymers in simulated body fluid (SBF) has been extensively applied to improve its biocompatibility, osteoconductivity, and osteoinductivity. Nevertheless, the development of an uniform distributed and deep controllable bone-like apatite in the natural polymers is still not satisfactory [46,47]. In the study, we have integrated several technologies to achieve full-thickness mineralization in the microgels. First, lyophilization techniques were introduced to obtain porous structures in the microgels. Pore structure could be observed under the microscope (red arrowheads) (Fig. 2B, S1A), and the pore size varied from 80 μm to 150 μm (Fig. 3F), which could guarantee adequate SBF infiltration and ion exchange [23]. Second, the abundant functional groups (hydroxyl and carboxyl groups) on GO made it possible to cross-link with hydrogels and provide more bioactive sites for ions deposition, prenucleation crystals formation, and continued crystals growth [48]. Third, according to our previous study, the depth of bone-like apatite growth into the GO-Col scaffolds was varied from 239 to 348 μm [5]. We used the microarray chips to develop three types of microgels (500 μm, 1000 μm, and 1500 μm) to fabricate the multi-layered microgels. These sizes ensured that the bone-like apatites could reach the deepest part of each layer (Fig. 3A–B).

In the study, the multi-layer mineralized GO-Col-HAp microgels showed time-dependent proliferation and favorable osteogenic differentiation of rBMSCs in vitro (Figs. 4–5). These results might be due to the following reasons: (1) The porous structure of the microgels possessed a good nutrient and oxygen exchange efficiency, contributing to a favorable microenvironment for cell proliferation [4]. Moreover, appropriate pore size and roughness surface are more conducive to cell adherence and migration [49]. These relative small pore sizes offer a larger surface area and provide a certain ligand density that affects the integrin-binding after initial seeding. These characteristics ultimately promote the cell attachment, migration and growth [50]. (2) The incorporation of GO provided more bioactive sites for HAp deposition and proteins adsorption, which could promoted cell adhesion and proliferation [51]. (3) Owing to the full-thickness distribution of HAp, the multi-layer mineralized microgels can continuously release Ca and P elements to promote the migration of stem cells into the inner regions and strengthen osteogenesis [52].

The mechanical properties of hydrogels have been reported to play an important role in determining cell fate [53,54]. Sufficient mechanical strength was necessary to ensure the structural integrity of the hydrogels and to resist stress in the bone defect area. In this study, the elastic modulus of the multi-layer mineralized GO-Col-HAp microgels was 1.95 ± 0.05 MPa, which was higher than other groups (Fig. 3I). These good mechanical strengths of MMGCH microgels contributed to good osteogenic differentiation in vitro and favorable bone regeneration effects in vivo (Figs. 5–6). The complete structure was observed at the early stage of implantation, which guaranteed the host cells (such as mesenchymal

stem cells, progenitor cells, and osteoblasts [2,55,56]) rapidly grew into the microgels and resulted in the formation of new bone (Figs. 7–8). The good mechanical strength might be due to the following reasons: (1) In terms of hydrogels composition, the GO possessed good mechanical strength [57]. The cooperation of GO into hydrogels can enhance the mechanical properties through adequate cross-linking. (2) Structurally, the multi-layer mineralized structure mimicked the structure of pearl and acted as "brick-to-mortar" to consolidate porous structures. The skeleton formed by the Col-GO can be referred to as "brick", and the biomineralization of HAp in the hydrogels can be referred to as "mortar". The multi-encapsulation of hydrogels with 500 μm, 1000 μm, and 1500 μm diameters can be regarded as the growth of a pearl.

To confirm the bone regeneration effect of microgels, we used the cranial and mandibular bone defect models, which were difficult to fix artificial bone substitutes in clinical [58–62]. The mechanical strength of the MMGCH microgels was 1.55 MPa ± 0.07 MPa (Fig. 3I), which was sufficient for these non-load-bearing bone defects. In the study, the cranial bone defects in the MMGCH group were almost fully filled with newly formed dense bone tissue after 12 weeks of implantation. The mandibular bone defects in the MMGCH group also exhibited more bone tissues than the other two groups (Figs. 6–8). The possible in vivo bone regeneration process could be illustrated below. The defect regions existed many host-derived cells, such as mesenchymal stem cells, progenitor cells, and osteoblasts. These host-derived cells were mainly distributed in the dura mater and host bone. After placing the microgels at the defect site, the host-derived cells rapidly grew into the microgels due to the suitable environment provided by the porous structure and multi-layer mineralized HAp. In the early stages of bone regeneration, recruitment and redistribution of host cells resulted in the formation of new bone at the defect margins and the interface between the microgel and the dura mater. When the implantation time was prolonged to 12 weeks, more bone tissues were formed in the microgels due to the favorable nutrient supply and oxygen exchange provided by the microstructures of the microgels. Finally, the bone tissues in the microgels extended outward, joined together, and completely filled the defect region. The multi-layer mineralized microgels played a vital role in the whole process, including providing physical support, absorbing host-derived cells and proteins, and providing a favorable osteogenic environment.

Although GO has exhibited attractive advantages in bone regeneration, there are still some concerns about its potential toxicity [63]. The current studies indicate that the potential toxicity of GO is related to its size, concentration, functionalization, and fabricated structure [64]. In the study, GO could be observed in the defect regions, and part of the microgels was substituted by the regenerated bone tissues. What's more, no obvious inflammation was observed (Figs. 7–8). This good biocompatibility and low cytotoxicity of GO-based microgels could be explained by the following reasons: (1) The concentration of GO (1 mg/mL) in the microgels was lower than the toxicity dose (100 mg/mL) [5]. (2) The GO was functionalized by the hydrogels through the chemical bond. This functionalized GO was stable and barely penetration into the cell membrane [65]. (3) When the GO-based hydrogels were implanted into the body, the microgels could be probably wrapped by the newly formed bone tissues, resulting in preventing or reducing the spread of residues to other tissues or organs. On the other hand, the GO-based hydrogels could be biodegraded through the action of horseradish peroxidase (HRP) and myeloperoxidase (MPO), followed by taking up by macrophages, and finally excreted out of the body through renal and lungs [4,66].

5. Conclusions

In summary, this study successfully fabricated a pearl-inspired and multi-layer mineralized GO-Col-HAp microgels (MMGCH) through microarray chips and multiple encapsulations. These pearl-inspired microgels exhibited efficient nutrient exchange to promote cell proliferation and uniform HAp distribution, significantly strengthening the

osteogenic effect of hydrogels. Moreover, the in vivo studies validated the satisfactory bone regeneration efficiency both in the cranial and mandibular defects. Thus, this well-fabricated method has the potential of uniformly distributing HAp microgels for bone regeneration and bionic construction.

Credit author statement

Chuchao Zhou: Conceptualization, Methodology, Data curation, Writing - original draft. Chao Luo: Data curation, Methodology. Shaokai Liu: Data curation, Software. Shangxuan Jiang: Data curation. Xin Liu: Data curation. Jialun Li: Software, Visualization. Xinyue Zhang:Data curation, Methodology. Xiaoyan Wu: Data curation. Jiaming Sun: Supervision, Writing - review & editing. Zhenxing Wang: Writing - review & editing, Project administration.

Declaration of competing interest

The authors declare that they have no known competing financial interests or personal relationships that could have appeared to influence the work reported in this paper.

Acknowledgments

Supplementary data

Supplementary data to this article is available.

Appendix A. Supplementary data

Supplementary data to this article can be found online at https://doi.org/10.1016/j.mtbio.2022.100307.

References

[1] C. Garot, G. Bettega, C. Picart, Adv. Funct. Mater. 31 (5) (2021) 2006967, https://doi.org/10.1002/adfm.202006967.
[2] S.J. Wang, et al., Adv. Mater. 31 (49) (2019), e1904341, https://doi.org/10.1002/adma.201904341.
[3] A. Marrella, et al., Mater. Today 21 (4) (2018) 362–376, https://doi.org/10.1016/j.mattod.2017.10.005.
[4] K. Zhou, et al., ACS Nano 13 (8) (2019) 9595–9606, https://doi.org/10.1021/acsnano.9b04723.
[5] C. Zhou, et al., ACS Appl. Mater. Interfaces 10 (50) (2018) 44080–44091, https://doi.org/10.1021/acsami.8b17636.
[6] J. Zhang, et al., Adv. Mater. 29 (17) (2017) 1605546, https://doi.org/10.1002/adma.201605546, n/a.
[7] S. Liu, et al., ACS Appl. Mater. Interfaces (2018), https://doi.org/10.1021/acsami.8b11071.
[8] D. Zhang, et al., Bioact. Mater. 3 (1) (2018) 129–138, https://doi.org/10.1016/j.bioactmat.2017.08.004.
[9] X.W.Z.Y. Jing Ruan, Adv. Funct. Mater. 26 (2016) 1085–1097, https://doi.org/10.1002/adfm.201504141.
[10] C. Zhang, et al., Biomater. Sci.-UK 9 (6) (2021) 2146–2161, https://doi.org/10.1039/D0BM01963A.
[11] S. Liu, et al., Mater. Sci. Eng. C 105 (2019) 110137, https://doi.org/10.1016/j.msec.2019.110137.
[12] Y. Wu, et al., Nat. Commun. 11 (1) (2020) 1182, https://doi.org/10.1038/s41467-020-14716-z, 1182.
[13] N.M. Bardhan, et al., ACS Nano 11 (2) (2017) 1548–1558, https://doi.org/10.1021/acsnano.6b06979.
[14] M. Sari, et al., Biomater. Res. 25 (1) (2021), https://doi.org/10.1186/s40824-021-00203-z.
[15] W.E.G. Müller, et al., Acta Biomater. 118 (2020) 233–247, https://doi.org/10.1016/j.actbio.2020.10.023.
[16] X. Mi, et al., ACS Appl. Mater. Interfaces 12 (29) (2020) 32503–32513, https://doi.org/10.1021/acsami.0c11003.
[17] Y. Li, et al., ACS Biomater. Sci. Eng. 6 (1) (2020) 320–328, https://doi.org/10.1021/acsbiomaterials.9b00914.

[18] S. Bu, et al., ACS Appl. Mater. Interfaces 12 (11) (2020) 12468–12477, https://doi.org/10.1021/acsami.9b22559.
[19] A.G.S. Ali, et al., Biomed. Mater. 13 (5) (2018), 055005, https://doi.org/10.1088/1748-605X/aac7a5.
[20] P. Mullick, G. Das, R. Aiyagari, Mater. Sci. Eng. C 126 (2021) 112101, https://doi.org/10.1016/j.msec.2021.112101, 112101.
[21] J. Lee, et al., Materials 11 (9) (2018) 1711, https://doi.org/10.3390/ma11091711.
[22] M. Degli Esposti, et al., Mater. Sci. Eng. C 100 (2019) 286–296, https://doi.org/10.1016/j.msec.2019.03.014.
[23] K. Shin, et al., Tissue Eng Part A, 2017, https://doi.org/10.1089/ten.TEA.2016.0556.
[24] T. Li, et al., Adv. Healthc. Mater. 9 (4) (2020), e1901211, https://doi.org/10.1002/adhm.201901211 n/a.
[25] C.S. Lee, et al., Adv. Funct. Mater. 30 (43) (2020) 2003717, https://doi.org/10.1002/adfm.202003717.
[26] Q. Cheng, C. Huang, A.P. Tomsia, Adv. Mater. 29 (45) (2017) 1703155, https://doi.org/10.1002/adma.201703155.
[27] G. Tan, et al., Adv. Mater. 31 (52) (2019), e1904603, https://doi.org/10.1002/adma.201904603.
[28] H. Zhao, L. Guo, Adv. Mater. 29 (45) (2017) 1702903, https://doi.org/10.1002/adma.201702903.
[29] S. Qiu, et al., ACS Appl. Mater. Interfaces 12 (32) (2020) 36639–36651, https://doi.org/10.1021/acsami.0c09685.
[30] K. Liang, et al., ACS Nano 14 (11) (2020) 14731–14739, https://doi.org/10.1021/acsnano.0c00913.
[31] J. Xue, et al., Acta Biomater. 100 (2019) 270–279, https://doi.org/10.1016/j.actbio.2019.10.012.
[32] D. Wei, J. Dao, G. Chen, Adv. Mater. 30 (31) (2018) 1802273, https://doi.org/10.1002/adma.201802273.
[33] F. Ding, et al., Sci. Adv. 3 (7) (2017), e1701212, https://doi.org/10.1126/sciadv.1701212 e1701212.
[34] P. Feng, et al., Adv. Sci. 5 (6) (2018) 1700817, https://doi.org/10.1002/advs.201700817, n/a.
[35] H.Y. Mi, et al., Chem. Eng. J. 348 (2018) 786–798, https://doi.org/10.1016/j.cej.2018.04.198.
[36] D. Chen, H. Feng, J. Li, Chem. Rev. 112 (11) (2012) 6027–6053, https://doi.org/10.1021/cr300115g.
[37] C. Luo, et al., Theranostics 9 (16) (2019) 4663–4677, https://doi.org/10.7150/thno.34464.
[38] S. Liu, et al., ACS Appl. Mater. Interfaces 10 (49) (2018) 42948–42958, https://doi.org/10.1021/acsami.8b11071.
[39] C. Torres-Sanchez, et al., Mater. Sci. Eng. Mater. Biol. Appl. 124 (2021) 112026, https://doi.org/10.1016/j.msec.2021.112026.
[40] M. Wu, et al., Int. J. Biol. Macromol. 162 (2020) 1627–1641, https://doi.org/10.1016/j.ijbiomac.2020.08.029.
[41] Y. Zeng, et al., Bioact. Mater. 5 (4) (2020) 859–870, https://doi.org/10.1016/j.bioactmat.2020.06.010.
[42] S. Orrego, et al., Adv. Mater. 32 (21) (2020), e1906970, https://doi.org/10.1002/adma.201906970.
[43] Y. Xu, et al., Nat. Commun. 11 (1) (2020) 5068, https://doi.org/10.1038/s41467-020-18846-2.
[44] D. Jiao, et al., Bioact. Mater. 6 (7) (2021) 2011–2028, https://doi.org/10.1016/j.bioactmat.2020.12.003.
[45] E.M. Gerhard, et al., Acta Biomater. 54 (2017) 21–34, https://doi.org/10.1016/j.actbio.2017.03.003.
[46] S. Chen, et al., Sci. Adv. 7 (31) (2021), https://doi.org/10.1126/sciadv.abg3089.
[47] S. Bu, et al., ACS Appl. Mater. Interfaces 12 (11) (2020) 12468–12477, https://doi.org/10.1021/acsami.9b22559.
[48] Z. Li, et al., Biomaterials 277 (2021) 121082, https://doi.org/10.1016/j.biomaterials.2021.121082.
[49] M. Lian, et al., Biomaterials 274 (2021) 120841, https://doi.org/10.1016/j.biomaterials.2021.120841.
[50] C. Torres-Sanchez, et al., Mater. Sci. Eng. C 77 (2017) 219–228, https://doi.org/10.1016/j.msec.2017.03.249.
[51] J. Wu, et al., Int. J. Nanomed. 14 (2019) 733–751, https://doi.org/10.2147/IJN.S187664.
[52] Z. Li, et al., Bioact. Mater. 6 (11) (2021) 4053–4064, https://doi.org/10.1016/j.bioactmat.2021.04.014.
[53] A.E. Jakus, et al., Sci. Transl. Med. 8 (358) (2016), https://doi.org/10.1126/scitranslmed.aaf7704, 358ra127-358ra127.
[54] R. Li, et al., Bioact. Mater. 3 (3) (2018) 322–333, https://doi.org/10.1016/j.bioactmat.2017.12.001.
[55] M. Zhai, et al., Adv. Sci. 7 (19) (2020) 2001334, https://doi.org/10.1002/advs.202001334, n/a.
[56] M. Dang, et al., Biomaterials 114 (2017) 1–9, https://doi.org/10.1016/j.biomaterials.2016.10.049.
[57] H. Luo, et al., Nano-Micro Lett. 10 (3) (2018), https://doi.org/10.1007/s40820-018-0195-3.
[58] P. Lohmann, et al., Biomaterials 113 (2016) 158–169, https://doi.org/10.1016/j.biomaterials.2016.10.039.
[59] W. Zhang, et al., Biofabrication 12 (3) (2020), 035020, https://doi.org/10.1088/1758-5090/ab906e.
[60] C. Shuai, et al., Nano Energy 74 (2020) 104825, https://doi.org/10.1016/j.nanoen.2020.104825.
[61] C. Shuai, et al., Chem. Eng. J. 374 (2019) 304–315, https://doi.org/10.1016/j.cej.2019.03.273.

[62] Y. Jiang, et al., Nano Today 39 (2021) 101182, https://doi.org/10.1016/j.nantod.2021.101182.

[63] A.M. Diez-Pascual, A.L. Diez-Vicente, ACS Appl. Mater. Interfaces 8 (28) (2016) 17902–17914, https://doi.org/10.1021/acsami.6b05635.

[64] Z. Du, et al., Int. J. Nanomed. 15 (2020) 7523–7551, https://doi.org/10.2147/IJN.S271917.

[65] A. Diez-Pascual, Polym. Bull. 9 (12) (2017) 260, https://doi.org/10.3390/polym9070260.

[66] R. Kurapati, et al., Angew. Chem. Int. Ed. 57 (36) (2018) 11722–11727, https://doi.org/10.1002/anie.201806906.